

LETTER TO THE EDITOR

K2-399 b is not a planet

The Saturn that wandered through the Neptune desert is actually a hierarchical eclipsing binary[★]

J. Lillo-Box^{1,★,✉}, D. W. Latham², K. A. Collins², D. J. Armstrong^{3,4,✉}, D. Gandolfi^{5,✉}, E. L. N. Jensen^{6,✉}, A. Castro-González^{1,✉}, O. Balsalobre-Ruza^{1,✉}, B. Montesinos^{1,✉}, S. G. Sousa^{7,✉}, J. Aceituno⁸, R. P. Schwarz^{2,✉}, N. Narita^{9,10,11,✉}, A. Fukui^{9,11}, J. Cabrera¹², A. Hadjigeorgiou³, M. Kuzuhara^{10,13,✉}, T. Hirano^{10,13,✉}, M. Fridlund^{14,15}, A. P. Hatzes^{16,✉}, O. Barragán¹⁷, and N. M. Batalha¹⁸

(Affiliations can be found after the references)

Received 5 July 2024 / Accepted 21 August 2024

ABSTRACT

Context. The transit technique has been very efficient over the past decades in detecting planet-candidate signals. The so-called statistical validation approach has become a popular way of verifying a candidate's planetary nature. However, the incomplete consideration of false-positive scenarios and data quality can lead to misinterpretation of the results.

Aims. In this work, we revise the planetary status of K2-399 b, a validated planet with an estimated false-positive probability of 0.078% located in the middle of the so-called Neptunian desert, and hence a potential key target for atmospheric prospects.

Methods. We used radial velocity data from the CARMENES, HARPS, and TRES spectrographs, as well as ground-based multiband transit photometry provided by LCOGT MuSCAT3 and broad band photometry to test the planetary scenario.

Results. Our analysis of the available data does not support the existence of this (otherwise key) planet, and instead points to a scenario composed of an early G-dwarf orbited –with a period of a $846.62^{+0.22}_{-0.28}$ days– by a pair of eclipsing M-dwarfs (hence a hierarchical eclipsing binary) likely in the mid-type domain. We thus demote K2-399 b as a planet.

Conclusions. We conclude that the validation process, while very useful to prioritize follow-up efforts, must always be conducted with careful attention to data quality while ensuring that all possible scenarios have been properly tested to get reliable results. We also encourage developers of validation algorithms to ensure the accuracy of a priori probabilities for different stellar scenarios that can lead to this kind of false validation. We further encourage the use of follow-up observations when possible (such as radial velocity and/or multiband light curves) to confirm the planetary nature of detected transiting signals rather than only relying on validation tools.

Key words. techniques: photometric – techniques: radial velocities – planets and satellites: detection – planets and satellites: fundamental parameters – planets and satellites: individual: K2-399

1. Introduction

After the launch of the *Kepler* mission (Borucki et al. 2010), the first Earth-size and sub-Earth-size planets were detected with the transit technique (e.g., Batalha et al. 2011; Barclay et al. 2013; Sanchis-Ojeda et al. 2013). In contrast to gas giants, the radial velocity (RV) signature of the small planets detected by *Kepler* was out of reach of high-precision ultrastable spectrographs owing to the faintness of most *Kepler* host stars ($V > 13$), which made RV follow-up observations difficult. In this context, the validation process was proposed (Torres et al. 2011; Fressin et al. 2011; Morton & Johnson 2011), which consists of the statistical rejection of alternative nonplanetary

scenarios that could reproduce the observed transit signal. Based on the transit properties (e.g., duration and shape), and optionally fed by ancillary observations, such as low-precision RV data or high-spatial-resolution imaging, the proposed algorithms can determine an overall probability that the transit signal comes from another nonplanetary scenario, known as the false positive probability (FPP). Different authors have, over the years, established different thresholds to consider a transit signal as a validated planet (e.g., Torres et al. 2015; Rowe et al. 2014; Morton et al. 2016; Armstrong et al. 2021; Mantovan et al. 2022; Castro-González et al. 2022).

Depending on the different catalogs, this validated disposition is directly put at the same level as the so-called confirmation process (typically involving a mass measurement for the planet). As an example, the NASA Exoplanet Archive¹ (Akeson et al. 2013) or the exoplanets.eu² (Schneider et al. 2011) catalogs, being the two most relevant in the field, do not distinguish among these two different dispositions. This may have key implications in population synthesis studies and several other follow-up

[★] This work is based on observations collected (a) at the Centro Astronómico Hispano en Andalucía (CAHA) at Calar Alto, operated jointly by the Instituto de Astrofísica de Andalucía (CSIC) and the Junta de Andalucía; (b) at the European Southern Observatory (ESO) under ESO programmes 0100.C-0808 and 108.21YY; (c) at Roque de los Muchachos Observatory with the Italian Telescopio Nazionale Galileo (TNG) operated by the INAF – Fundación Galileo Galilei, under the OPTICON program 2017B/059.

^{**} Corresponding author; Jorge.Lillo@cab.inta-csic.es

¹ <https://exoplanetarchive.ipac.caltech.edu>

² <https://exoplanet.eu/home/>

observing programs. In this context, an exoplanet confirmation protocol needs to be discussed among the exoplanet community to agree on the principles that qualify a planet detection as confirmed. Revising the validation process and establishing a confirmation protocol will be of especial relevance in the context of the new PLATO mission (Rauer et al. 2014) and forthcoming facilities such as the ELT, the Habitable Worlds Observatory (HWO), and the proposed mission LIFE (Quanz et al. 2022).

K2-399 b was presented by Zink et al. (2021) as a planet candidate based on data from the repurposed version of the *Kepler* mission, K2 (Howell et al. 2014). The authors identified a transit signal with an ultrashort period of ~ 0.76 days and a planet-to-star radius ratio of ~ 0.035 (corresponding to $\sim 6 R_{\oplus}$ for the derived stellar parameters resulting in an F9 dwarf), with a grazing eclipse of impact parameter ~ 0.97 . According to the stellar properties derived in this discovery paper, the semi-major axis of the planet candidate orbit was only ~ 1.9 times the stellar radius, becoming one of the closest planets to its parent star. More interestingly, its size and period meant that this planet belonged to the so-far-unpopulated Saturn and Neptune desert (Benítez-Llambay et al. 2011; Szabó & Kiss 2011; Youdin 2011), a key region of the parameter space sculpted by formation and migration processes that is still under debate (e.g., Castro-González et al. 2024).

The planet candidate was subsequently validated by Christiansen et al. (2022) using the *vespa*³ code (Morton 2012, 2015). The authors used high-resolution spectra and high-spatial-resolution imaging to feed this algorithm, and obtained an FPP of 7.8×10^{-4} , thus validating the signal as having a planetary origin. It is interesting to note that the authors point out the high *Gaia* (Gaia Collaboration 2016) *ruwe*⁴ value of this star, of namely 5.89 (where values above 1.4 indicate a bad astrometric solution typically because of the presence of an unresolved star or a long-period substellar companion). However, their centroid motion analysis provided a high level of confidence that the transit occurs on-source. Consequently, the authors considered the signal as statistically validated. As such, this validated planet appears with the “Confirmed Planet” disposition in the NASA Exoplanet Archive⁵ and the “Confirmed” planet status in the *exoplanets.eu*⁶ catalog.

In this Letter, we provide additional follow-up observations (presented in Sect. 2), whose analysis in Sect. 3 allows us to demote the planetary status of this signal and to propose a more likely alternative scenario in Sect. 4. In Sect. 5, we conclude with some final remarks. Given the nature of this Letter, we use K2-399 b when referring to the claimed planet, and use the EPIC 248472140 naming convention to refer to the system.

2. Observations and stellar characterization

2.1. TRES spectroscopy

NASA’s Transiting Exoplanet Survey Satellite (TESS, Ricker et al. 2014) mission independently identified transit-like events in this star, named TIC 374200604 in the TESS Input Catalog, Stassun et al. 2019) and released it as TESS Object of Interest (TOI) TOI-4838 in early 2022. This led almost immediately to follow-up reconnaissance spectroscopy with

³ <https://github.com/timothydmorton/VESPA>

⁴ Renormalised Unit Weight Error.

⁵ <https://exoplanetarchive.ipac.caltech.edu/overview/K2-399>

⁶ https://exoplanet.eu/catalog/k2_399_b--9074/

the Tillinghast Reflector Echelle Spectrograph (TRES⁷, PI: A. Szentgyorgyi) on the 1.5-m Tillinghast Reflector at the Fred Lawrence Whipple Observatory on Mount Hopkins (Arizona, USA). TRES is a fiber-fed CCD spectrograph with a resolving power of $R = 44\,000$ and a wavelength coverage of 384 to 909 nm. The six TRES observations obtained for this target cover a wide time span of 2275 days and show large RV variations at the level of several km/s, with a median uncertainty per datapoint of 30 m/s. These RVs are listed in Table C.1.

2.2. HARPS and HARPS-N spectroscopy

The host star candidate K2-399 was selected as one of the key targets of the NOMADS (PI D. Armstrong; see, e.g., Osborn et al. 2023) and KESPRINT (PI: D. Gandolfi; see, e.g., Gandolfi et al. 2017) observing programs with the HARPS⁸ instrument at the 3.6-m telescope at La Silla Observatory (Chile) of the European Southern Observatory (ESO), before the candidate planet was validated. A total of 12 spectra were obtained through the KESPRINT program⁹ between 23 February 2018 and 15 March 2018, while 27 measurements were acquired through the NOMADS program¹⁰ from the 31 January 2023 to 28 April 2023. The whole dataset was reduced using the Data Reduction Software (DRS) version v3.8, and absolute RVs were extracted using the cross-correlation technique (Baranne et al. 1996) with a G2 mask. From the cross-correlation function (CCF) the RV, as well as the shape properties of the CCF (bisector span and FWHM) were obtained. The average RV uncertainty from this dataset is 7.0 m/s with a standard deviation of the uncertainties corresponding to 0.8 m/s. The RVs and activity and related indicators are shown in Table C.1. Two additional spectra were secured¹¹ with the HARPS-N spectrograph (Cosentino et al. 2012) mounted at the 3.58-m Telescopio Nazionale *Galileo* (TNG) of Roque de los Muchachos Observatory (La Palma, Spain). The data reduction and extraction of RVs are achieved following the same procedures as for the HARPS spectra.

2.3. CARMENES spectroscopy

We observed EPIC 248472140 in two campaigns with the CARMENES instrument (Quirrenbach et al. 2010) installed at the 3.5 m telescope at Calar Alto observatory. In the first campaign (PI: M. Kuzuhara), we acquired 20 measurements over four nights between 27 November 2018 and 26 February 2019. In our second campaign (PI: J. Lillo-Box) in 2024, on 7 January 2024 we carried out continuous monitoring of this star for 6 hours (one-third of the orbital period of K2-399 b), obtaining a total of ten spectra with an exposure time of 1800 s (two of them in-transit). Additionally, we obtained three datapoints on 3 February 2024, 17 February 2024, and 18 February 2024. All spectra were obtained with the Fabry-Pérot in fiber B to monitor the intra-night drift of the instrument. The data were reduced using standard procedures with the CARACAL¹² pipeline (Piskunov & Valenti 2002; Zechmeister et al.

⁷ <http://www.sao.arizona.edu/FLW0/60/tres.html>

⁸ High Accuracy Radial velocity Planet Searcher.

⁹ Program ID: 0100.C-0808.

¹⁰ Program ID: 108.21YY.

¹¹ This was part of the KESPRINT observing program (Program ID: OPT17B_59 or 2017B/059) of K2 transiting planet candidates (PI: A. P. Hatzes; see, e.g. Prieto-Arranz et al. 2018).

¹² CARMENES Reduction And CALibration.

2014), version 2.20. We use our own developed cross-correlation algorithm, SHAQ, developed for the K-dwarfs Orbiting By habitable Exoplanets experiment (KOBE, Lillo-Box et al. 2022), to extract the RVs, correct for the drift velocities, and obtain CCF properties like FWHM and BIS. We obtained absolute RVs with an average RV uncertainty of 8 m/s for the 2018 campaign and 16 m/s for the 2024 campaign. However, these RVs vary by several km/s within each campaign and by more than 10 km/s between both campaigns. We consider them as separate instruments for the RV analysis. The RVs and related indicators are shown in Table C.1.

2.4. MuSCAT3 multiwavelength photometry

We observed a full transit event window with the MuSCAT3 multiband imager (Narita et al. 2020) of K2-399 b on 30 March 2024 simultaneously in the four MuSCAT filters g , r , i , and z_s (having bandpasses 400–550, 550–700, 700–820, and 820–920 nm, respectively) from the Las Cumbres Observatory Global Telescope (LCOGT; Brown et al. 2013) 2 m Faulkes Telescope North at Haleakala Observatory on Maui, Hawai'i. All images were calibrated by the standard LCOGT BANZAI pipeline (McCully et al. 2018) and differential photometric data were extracted using AstroImageJ (Collins et al. 2017). We used circular photometric apertures of 5.1 arcsec, which excluded all of the flux from the nearest known neighbor in the *Gaia* DR3 catalog (*Gaia* DR3 3855957905329756416), which is ~ 47 arcsec west of our target star (see Fig. B.1). A V-shaped event was detected on-target with preliminary nominal depths at mid-transit of 0.18, 0.48, 1.21, and 2.28 ppt in g , r , i , and z_s bands, respectively, indicating that a fainter, much redder star is blended in the 5.1 arcsec follow-up photometric aperture and is hosting the eclipse. The light curves with preliminary models overplotted are shown in Figure 1 and the data are available on ExoFOP¹³.

2.5. Broad-band photometry

We retrieved the observed broad-band photometry of EPIC 248472140 from the Virtual Observatory SED Analyzer (VOSA, Bayo et al. 2008, 2014). In this process, we discarded several observations due to unknown uncertainties in their values. Table C.2 shows the photometry used and the corresponding band passes. The spectral energy distribution (SED) based on this photometry is shown in Fig. A.1.

2.6. Spectroscopic stellar characterization

We used a combined HARPS spectrum for EPIC 248472140 to estimate its stellar spectroscopic parameters (T_{eff} , $\log g$, microturbulence, [Fe/H]) using the ARES+MOOG methodology described in detail in Sousa et al. (2021), Sousa (2014), and Santos et al. (2013). Details on this spectroscopic characterization are provided in Appendix A.1. The results of this analysis led us to conclude that the dominant component of the spectrum in the visible range is a main sequence G1 dwarf star with an effective temperature of 5863 ± 62 K and a surface gravity of $\log g = 4.06 \pm 0.11$ dex. We also estimate a turbulent velocity of 1.111 ± 0.022 km/s and a metallicity of $[\text{Fe}/\text{H}] = 0.335 \pm 0.014$ dex. Based on these parameters and using the calibrations from Torres et al. (2010), we obtain a mass of $M_{\star,A} = 1.31 \pm 0.03 M_{\odot}$

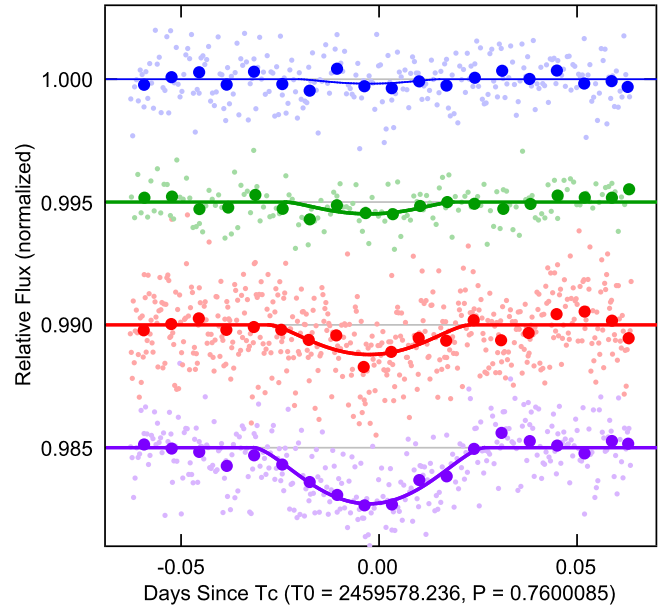


Fig. 1. LCOGT MuSCAT3 light curves of K2-399. The light curves from top to bottom are in the MuSCAT g , r , i , and z_s bands. The small symbols show the unbinned data and the larger symbols show the same data in ten-minute bins. The transit model fits are overplotted. A V-shaped event was detected on-target with depths at mid-transit of 0.18, 0.48, 1.21, and 2.28 ppt in g , r , i , and z_s bands, respectively, indicating that a fainter, much redder star is blended in the 5.1 arcsec follow-up photometric aperture and is hosting the eclipse.

and a radius of $R_{\star,A} = 1.57 \pm 0.05 R_{\odot}$. These results are shown in Table C.3.

3. Evidence for demoting K2-399 b as a planet

3.1. Radial velocity modeling

The RV data obtained from the different instruments display large variations at the level of several km/s. The generalized Lomb-Scargle (GLS, Zechmeister & Kürster 2009) periodogram of the dataset (accounting for the offsets resulting from the RV analysis described in this section) does not show any signal at the transiting period of 0.76 days (see top panel in Fig. B.2 and the marked dotted red vertical line). Instead, the largest power signal in the GLS periodogram corresponds to a signal in the range 830 to 900 days.

We modeled these RVs using the standard approach already presented in other, similar works (see, e.g., Lillo-Box et al. 2020). In this case, we use a Keplerian model parametrized by the orbital period (P), the time of conjunction (T_0), the eccentricity (e), the argument of periastron (ω), and the RV semi-amplitude (K). We also add an instrumental offset (δ_i) and a white noise term per instrument (jitter, σ_i).

We used the emcee code (Foreman-Mackey et al. 2013) to sample the posterior distribution of the parameters using a total of 44 walkers (four times the number of free parameters) and 50 000 steps per walker in a first burn-in phase. We then focus on a small ball around the maximum a posteriori N-dimensional parameter space and run a second chain with the same number of walkers and half of the steps (i.e. 25 000 steps). We checked for the convergence of the chains by requiring that the length of the chain be at least 50 times the autocorrelation time as suggested in the emcee documentation.

¹³ <https://exofop.ipac.caltech.edu/tess/target.php?id=374200604>

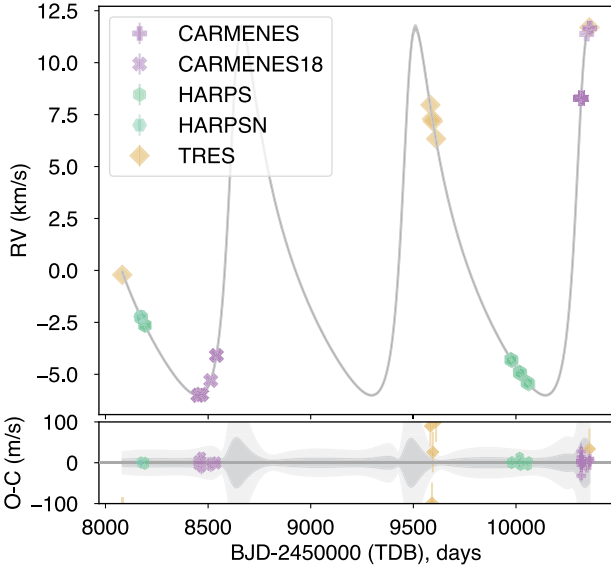


Fig. 2. Radial velocity time series (with the different instruments shown with different symbols and colors; see legend) and inferred RV model corresponding to the 1-Keplerian scenario.

The confidence intervals of the marginalised distributions of the parameters as well as the prior distributions used are shown in Table C.4. The chains converge to a solution corresponding to a Keplerian signal with a period of $P = 846.62^{+0.22}_{-0.28}$ days and an RV semi-amplitude of $K = 8.901^{+0.038}_{-0.050}$ km/s. The orbital architecture corresponds to an eccentric orbit of $e = 0.4919 \pm 0.0021$. These parameters correspond to a minimum mass of $0.4129 \pm 0.0066 M_{\text{J}}$ orbiting EPIC 248472140 A at the given periodicity and with a highly eccentric orbital architecture. The data and median model are shown in Fig. 2.

The overall root-mean-square (rms) of the residuals is 22 m/s, with no additional signals in the periodogram (see lower panel of Fig. B.2). In particular, no signal appears at the 0.76 days periodicity. Indeed, the rms values from the different instruments are 5 m/s (HARPS), 13 m/s (CARMENES), and 36 m/s (TRES). The uncertainties on the individual measurements of the most precise instruments (HARPS and CARMENES) are of the same order as this rms, and the expected RV semi-amplitude of the transiting planet candidate (estimated by Christiansen et al. 2022 based on empirical radius–mass relationships from Chen & Kipping 2017) was in the range of 20–30 m/s. Our CARMENES dataset includes one night covering one-third of this orbital period. If present around the main target, we should have detected its RV signal. Figure B.3 shows the residual RVs phase-folded at the 0.76 days period after subtracting the long-period Keplerian model, clearly showing no additional signals at the expected amplitude.

Hence, we can clearly conclude that this dataset does not support the existence of a signal at a periodicity of 0.76 days around the star EPIC 248472140 A, previously claimed to correspond to an ultrashort-period Saturn-like planet (K2-399 b). Indeed, by adding a second Keplerian signal to our model with tight priors on the period and time of conjunction from the transit signal, we can provide a maximum absolute mass for a transiting object around EPIC 248472140 A. By doing so, we can constrain the maximum RV amplitude at 0.76 days, corresponding to $K_{0.76\text{d}} < 3.85$ m/s (at 95% confidence level). This would correspond to a maximum planet mass of $6 M_{\oplus}$. This is however

incompatible with a planet having an inferred Saturn-like radius of $6 R_{\oplus}$ (as derived by Zink et al. 2021; Christiansen et al. 2022) whose expected mass is in the range of $32 \pm 22 M_{\oplus}$ according to the same authors.

3.2. Multiband photometry modeling

We analyzed the multiband photometry of the transit event observed by MuSCAT3 (see Sect. 2.4). Details of the modeling of this dataset are provided in Appendix A.3. From this analysis, we find a clear chromatic effect, with the depth of the eclipse going from $2.43^{+0.18}_{-0.22}$ parts per thousand (ppt) in the redder z_s band to being compatible with zero in the bluer g band; see Figs. 1 and A.2. We conclude that this clear chromaticity implies a significant amount of blending light from a source unrelated to the eclipsing pair. This chromaticity and its color dependence is consistent with the previous RV analysis and shows clear evidence that the eclipses are not occurring on the G1 dwarf star (being the diluting source) but instead on the long-period companion. See Appendix A.3 for details.

4. New proposed scenario

The evidence for demoting K2-399 b as a planet are clear from the analysis presented in Sect. 3. Here, we are curious to unveil the actual configuration of this system.

So far, we know that EPIC 248472140 has no chance-aligned companions as shown by the different high-spatial resolution images analyzed in Christiansen et al. (2022) and accessible through the ExoFOP (at least to their sensitivity limits). Additionally, we know from the RV analysis in Sect. 3.1 that the star is accompanied by a long-period stellar companion with a minimum mass of $0.41 M_{\text{J}}$. The RV analysis also reveals no variations at the periodicity of 0.76 days above 3.85 m/s at 95% confidence. From the multiband photometry described in Sect. 3.2 and Appendix A.3, we conclude that the transit presents a clear chromaticity, thus pointing to the long-period low-mass companion as the host of the transit events (see, e.g., Parviainen et al. 2019). Hence, we have three components in the system: the bright G1 dwarf star dominating the spectrum as shown in Sect. 2.6 (that we name *A*), a companion in a long-period orbit producing the large RV variations (*B*), and the object producing the eclipses in a short period (*C*).

From the RV analysis and multiband light curve analyses in Sect. 3.1, the eclipses are produced on component *B* and not on component *A* (see also Fig. B.3). The question then is what are the properties of the eclipsing components. The most extreme scenarios that accomplish a mass distribution in agreement with the RVs ($M_B \sin i + M_C \sin i = 0.41 M_{\text{J}}$) are as follows: (i) most of the mass is in one of the components (thus *B* being a \sim K7-M0 star¹⁴) with the eclipsing object *C* thus being either a grazing planet or a low-mass brown dwarf; or alternatively (ii) the mass is equally split between the two components ($M_B \sin i = M_C \sin i \approx 0.2 M_{\text{J}}$), and therefore the eclipses are produced by a pair of mid-type M-dwarfs (e.g., M5+M5). From the evidence that we provide in Appendix A.3 based on the multicolor analysis and in Appendix A.2 based on the SED analysis, we conclude that the second scenario is a significantly better representation of the data ($\chi^2 = 374$ versus $\chi^2 = 1402$), and that the system is composed of a G1 dwarf surrounded by a pair of similar-mass mid-type eclipsing M-dwarfs.

¹⁴ This accounts for some inclination different from 90° .

However, in this scenario, assuming the period of 0.76 days, a secondary eclipse should have been detected, while it has not. This opens two alternatives: either (1) the orbit is eccentric and is oriented so that we only see the primary eclipse; or (2) both components are of similar type (hence mass and radius), thus eclipsing each other and inducing same-depth eclipses but then with a period that is actually twice the reported value, that is, ~ 1.52 days. In Appendix A.5, we describe the evidence we have in favor of the second scenario and proving that the low-mass eclipsing binary accompanying EPIC 248472140 A has an orbital period twice that reported for K2-399 b (see also Fig. B.4). This could also be solved by detecting the RV signal of the eclipsing binary. Indeed, an M5 star at this distance would contribute a flux that is $10^{-2} - 10^{-3}$ times the flux from the main G1 star in the near-infrared (NIR) regime ($1-3 \mu\text{m}$). With high-signal-to-noise ratio (S/N) spectra in the near-infrared, the RV signal of the eclipsing binary could be detected. However, our data in the NIR have an average S/N per pixel of 15, thus preventing any study in this regard.

Finally, we also note that recently developed validation tools applied to this system also strongly favor the HEB scenario against the planet hypothesis (see Appendix A.6 for additional information).

5. Conclusions

We demonstrated with this work that the origin of the transit signals in EPIC 248472140 is not of a planetary nature as previously validated by Christiansen et al. (2022). Our RV data demonstrate the presence of a long-period component and the absence of the previously reported ultrashort-period signal around the main target. The multicolor transit photometry shows the nonplanetary origin of the eclipses, pointing to a low-mass binary, also suggested by the SED. This combined evidence points to a hierarchical triple system composed of an early G1-dwarf surrounded, on a long-period (~ 847 days) orbit, by a low-mass M-dwarf binary with a short period of ~ 1.52 days (instead of the reported 0.76 days) as the true scenario, revealing the reasons for misinterpretation of the transits as of planetary origin.

The previously confirmed planet K2-399 b is hence demoted to a false-positive hierarchical triple system. The analysis presented here, as well as in other previous works (e.g., Cabrera et al. 2017), demonstrates the clear need for a consensus on the definition of what we consider to be a confirmed planet. In this regard, we encourage the exoplanet community to develop an exoplanet confirmation protocol to define commonly accepted (technique-independent) generic principles to establish the “Confirmed” status of a detected signal.

Data availability

Full Table C.1 is available at the CDS via anonymous ftp to cdsarc.cds.unistra.fr (130.79.128.5) or via <https://cdsarc.cds.unistra.fr/viz-bin/cat/J/A+A/689/L8>

Acknowledgements. We thank the referee, Alexandre Santerne, for his thorough revision of this manuscript that has improved its final quality. J.L.-B. is funded by the Spanish Ministry of Science and Universities (MICIU/AEI/10.13039/501100011033/) and NextGenerationEU/PRTR grants PID2019-107061GB-C61 and CNS2023-144309. A.C.-G. is funded by the Spanish Ministry of Science through MCIN/AEI/10.13039/501100011033 grant PID2019-107061GB-C61. B.M. is funded by the former Spanish Ministry of Science and Innovation/State Agency of Research (MCIN/AEI/10.13039/501100011033/), grant PID2021-127289-NB-I00.

D.G. gratefully acknowledge the financial support from the grant for internationalization (GAND_GFI_23_01) provided by the University of Turin (Italy). This research has made use of the SVO Filter Profile Service “Carlos Rodrigo”, funded by MCIN/AEI/10.13039/501100011033/ through grant PID2020-112949GB-I00. This research was funded in part by the UKRI, (Grants ST/X001121/1, EP/X027562/1). We acknowledge a financial support from Astrobiology Center of NINS to obtain the observing time of CARMENES in 2019. This project has received funding from the European Union’s Horizon 2020 research and innovation programme under grant agreement No 730890 (OPTICON). This material reflects only the authors views and the Commission is not liable for any use that may be made of the information contained therein. This work benefited from the 2024 Exoplanet Summer Program in the Other Worlds Laboratory (OWL) at the University of California, Santa Cruz, a program funded by the Heising-Simons Foundation and NASA.” This research made use of the following software: *astropy*, (a community-developed core Python package for Astronomy, *Astropy Collaboration* 2013, 2018), *SciPy* (Virtanen et al. 2020), *matplotlib* (a Python library for publication quality graphics Hunter 2007), *astroML* (Vanderplas et al. 2012), *numpy* (Harris et al. 2020), and *AstroImageJ* (Collins et al. 2017), *TAPIR* (Jensen 2013), *exoplanet* (Foreman-Mackey et al. 2021a,b) and its dependencies (Agol et al. 2020; Kumar et al. 2019; Luger et al. 2019; Salviatier et al. 2016; Theano Development Team 2016). This research has made use of NASA’s Astrophysics Data System (ADS) Bibliographic Services, the SIMBAD database, operated at CDS, and the NASA Exoplanet Archive, which is operated by the California Institute of Technology, under contract with the National Aeronautics and Space Administration under the Exoplanet Exploration Program. We also used the data obtained from or tools provided by the portal exoplanet.eu of The Extrasolar Planets Encyclopaedia. This research has made use of the Exoplanet Follow-up Observation Program (ExoFOP; DOI: 10.26134/ExoFOP5) website, which is operated by the California Institute of Technology, under contract with the National Aeronautics and Space Administration under the Exoplanet Exploration Program. Funding for the TESS mission is provided by NASA’s Science Mission Directorate. KAC acknowledges support from the TESS mission via subaward s3449 from MIT. This work makes use of observations from the LCOGT network. This paper is based on observations made with the MuSCAT instruments, developed by the Astrobiology Center (ABC) in Japan, the University of Tokyo, and Las Cumbres Observatory (LCOGT). MuSCAT3 was developed with financial support by JSPS KAKENHI (JP18H05439) and JST PRESTO (JPMJPR1775), and is located at the Faulkes Telescope North on Maui, HI (USA), operated by LCOGT. MuSCAT4 was developed with financial support provided by the Heising-Simons Foundation (grant 2022-3611), JST grant number JPMJCR1761, and the ABC in Japan, and is located at the Faulkes Telescope South at Siding Spring Observatory (Australia), operated by LCOGT. This work is partly supported by JSPS KAKENHI Grant Numbers JP24H00017, JP24K00689 and JSPS Bilateral Program Number JPJSBP120249910. We are extremely grateful to the ESO and TNG staff members for their unique and superb support during the observations.

References

- Agol, E., Luger, R., & Foreman-Mackey, D. 2020, *AJ*, **159**, 123
 Akeson, R. L., Chen, X., Ciardi, D., et al. 2013, *PASP*, **125**, 989
 Aller, A., Lillo-Box, J., Jones, D., Miranda, L. F., & Barceló Forzeza, S. 2020, *A&A*, **635**, A128
 Anglada-Escudé, G., & Butler, R. P. 2012, *ApJS*, **200**, 15
 Armstrong, D. J., Gamper, J., & Damoulas, T. 2021, *MNRAS*, **504**, 5327
 Astropy Collaboration (Robitaille, T. P., et al.) 2013, *A&A*, **558**, A33
 Astropy Collaboration (Price-Whelan, A. M., et al.) 2018, *AJ*, **156**, 123
 Baranne, A., Queloz, D., Mayor, M., et al. 1996, *A&AS*, **119**, 373
 Barclay, T., Rowe, J. F., Lissauer, J. J., et al. 2013, *Nature*, **494**, 452
 Batalha, N. M., Borucki, W. J., Bryson, S. T., et al. 2011, *ApJ*, **729**, 27
 Bayo, A., Rodrigo, C., Barrado Y Navascués, D., et al. 2008, *A&A*, **492**, 277
 Bayo, A., Rodrigo, C., Barrado, D., et al. 2014, *ASI Conf. Ser.*, **11**, 93
 Benítez-Llambay, P., Masset, F., & Beaugé, C. 2011, *A&A*, **528**, A2
 Borucki, W. J., Koch, D., Basri, G., et al. 2010, *Science*, **327**, 977
 Brown, T. M., Baliber, N., Bianco, F. B., et al. 2013, *PASP*, **125**, 1031
 Cabrera, J., Barros, S. C. C., Armstrong, D., et al. 2017, *A&A*, **606**, A75
 Castro-González, A., Díez Alonso, E., Menéndez Blanco, J., et al. 2022, *MNRAS*, **509**, 1075
 Castro-González, A., Bourrier, V., Lillo-Box, J., et al. 2024, *A&A*, **689**, A250
 Chen, J., & Kipping, D. 2017, *ApJ*, **834**, 17
 Christiansen, J. L., Bhure, S., Zink, J. K., et al. 2022, *AJ*, **163**, 244
 Collins, K. A., Kielkopf, J. F., Stassun, K. G., & Hessman, F. V. 2017, *AJ*, **153**, 77
 Cosentino, R., Lovis, C., Pepe, F., et al. 2012, *SPIE Conf. Ser.*, **8446**, 1

- Covey, K. R., Ivezić, Ž., Schlegel, D., et al. 2007, *AJ*, **134**, 2398
- da Silva, L., Girardi, L., Pasquini, L., et al. 2006, *A&A*, **458**, 609
- Foreman-Mackey, D., Hogg, D. W., Lang, D., & Goodman, J. 2013, *PASP*, **125**, 306
- Foreman-Mackey, D., Luger, R., Agol, E., et al. 2021a, *J. Open Source Softw.*, **6**, 3285
- Foreman-Mackey, D., Savel, A., Luger, R., et al. 2021b, <https://doi.org/10.5281/zenodo.1998447>
- Fressin, F., Torres, G., Désert, J.-M., et al. 2011, *ApJS*, **197**, 5
- Gaia Collaboration (Prusti, T., et al.) 2016, *A&A*, **595**, A1
- Gandolfi, D., Barragán, O., Hatzes, A. P., et al. 2017, *AJ*, **154**, 123
- Gelman, A., & Rubin, D. B. 1992, *Stat. Sci.*, **7**, 457
- Giacalone, S., Dressing, C. D., Hedges, C., et al. 2022, *AJ*, **163**, 99
- Hadjigeorgiou, A., & Armstrong, D. J. 2023, *MNRAS*, **527**, 4018
- Harris, C. R., Millman, K. J., van der Walt, S. J., et al. 2020, *Nature*, **585**, 357
- Hauschildt, P. H., Allard, F., & Baron, E. 1999, *ApJ*, **512**, 377
- Hoffman, M. D., & Gelman, A. 2014, *J. Mach. Learn. Res.*, **15**, 1593
- Howell, S. B., Sobek, C., Haas, M., et al. 2014, *PASP*, **126**, 398
- Hunter, J. D. 2007, *Comput. Sci. Eng.*, **9**, 90
- Jensen, E. 2013, Astrophysics Source Code Library [record ascl:1306.007]
- Kumar, R., Carroll, C., Hartikainen, A., & Martin, O. A. 2019, *The J. Open Source Softw.*, **4**, 1143
- Kurucz, R. L. 1993, *SYNTHE spectrum synthesis programs and line data*, Kurucz CD-ROM No. 18 (Cambridge, Mass.: Smithsonian Astrophysical Observatory)
- Lillo-Box, J., Lopez, T. A., Santerne, A., et al. 2020, *A&A*, **640**, A48
- Lillo-Box, J., Santos, N. C., Santerne, A., et al. 2022, *A&A*, **667**, A102
- Luger, R., Agol, E., Foreman-Mackey, D., et al. 2019, *AJ*, **157**, 64
- Mantovan, G., Montalto, M., Piotto, G., et al. 2022, *MNRAS*, **516**, 4432
- McCully, C., Volgenau, N. H., Harbeck, D.-R., et al. 2018, *SPIE Conf. Ser.*, **10707**, 107070K
- Morton, T. D. 2012, *ApJ*, **761**, 6
- Morton, T. D. 2015, Astrophysics Source Code Library [record ascl:1503.011]
- Morton, T. D., & Johnson, J. A. 2011, *ApJ*, **738**, 170
- Morton, T. D., Bryson, S. T., Coughlin, J. L., et al. 2016, *ApJ*, **822**, 86
- Morton, T. D., Giacalone, S., & Bryson, S. 2023, *Res. Notes AAS*, **7**, 107
- Narita, N., Fukui, A., Yamamuro, T., et al. 2020, *SPIE Conf. Ser.*, **11447**, 114475K
- Osborn, A., Armstrong, D. J., Fernández Fernández, J., et al. 2023, *MNRAS*, **526**, 548
- Parviainen, H., Tingley, B., Deeg, H. J., et al. 2019, *A&A*, **630**, A89
- Piskunov, N. E., & Valenti, J. A. 2002, *A&A*, **385**, 1095
- Prieto-Arranz, J., Palle, E., Gandolfi, D., et al. 2018, *A&A*, **618**, A116
- Quanz, S. P., Ottiger, M., Fontanet, E., et al. 2022, *A&A*, **664**, A21
- Quirrenbach, A., Amado, P. J., Mandel, H., et al. 2010, *ASP Conf. Ser.*, **430**, 521
- Rauer, H., Catala, C., Aerts, C., et al. 2014, *Exp. Astron.*, **38**, 249
- Ricker, G. R., Winn, J. N., Vanderspek, R., et al. 2014, *SPIE Conf. Ser.*, **9143**, 20
- Rodrigo, C., & Solano, E. 2020, in *XIV.0 Scientific Meeting (virtual) of the Spanish Astronomical Society*, 182
- Rodrigo, C., Solano, E., & Bayo, A. 2012, in *SVO Filter Profile Service Version 1.0, IVOA Working Draft 15 October 2012*
- Rodrigo, C., Cruz, P., Aguilar, J. F., et al. 2024, *A&A*, **689**, A93
- Rowe, J. F., Bryson, S. T., Marcy, G. W., et al. 2014, *ApJ*, **784**, 45
- Salvatier, J., Wiecki, T. V., & Fonnesbeck, C. 2016, *PeerJ Comput. Sci.*, **2**, e55
- Sanchis-Ojeda, R., Winn, J. N., Marcy, G. W., et al. 2013, *ApJ*, **775**, 54
- Santos, N. C., Sousa, S. G., Mortier, A., et al. 2013, *A&A*, **556**, A150
- Schneider, J., Dedieu, C., Le Sidaner, P., Savalle, R., & Zolotukhin, I. 2011, *A&A*, **532**, A79
- Snedden, C. A. 1973, Ph.D. Thesis, The University of Texas at Austin, USA
- Sousa, S. G. 2014, *ARES + MOOG: A Practical Overview of an Equivalent Width (EW) Method to Derive Stellar Parameters*, 297
- Sousa, S. G., Santos, N. C., Israelian, G., Mayor, M., & Monteiro, M. J. P. F. G. 2007, *A&A*, **469**, 783
- Sousa, S. G., Santos, N. C., Mayor, M., et al. 2008, *A&A*, **487**, 373
- Sousa, S. G., Santos, N. C., Adibekyan, V., Delgado-Mena, E., & Israelian, G. 2015, *A&A*, **577**, A67
- Sousa, S. G., Adibekyan, V., Delgado-Mena, E., et al. 2021, *A&A*, **656**, A53
- Stassun, K. G., Oelkers, R. J., Paegert, M., et al. 2019, *AJ*, **158**, 138
- Szabó, G. M., & Kiss, L. L. 2011, *ApJ*, **727**, L44
- Theano Development Team 2016, ArXiv e-prints [arXiv:1605.02688]
- Tonry, J. L., Stubbs, C. W., Lykke, K. R., et al. 2012, *ApJ*, **750**, 99
- Torres, G., Andersen, J., & Giménez, A. 2010, *A&ARv.*, **18**, 67
- Torres, G., Fressin, F., Batalha, N. M., et al. 2011, *ApJ*, **727**, 24
- Torres, G., Kipping, D. M., Fressin, F., et al. 2015, *ApJ*, **800**, 99
- Vanderplas, J., Connolly, A., Ivezić, Ž., & Gray, A. 2012, in *Conference on Intelligent Data Understanding (CIDU)*, 47
- Virtanen, P., Gommers, R., Oliphant, T. E., et al. 2020, *Nat. Methods*, **17**, 261
- Youdin, A. N. 2011, *ApJ*, **742**, 38
- Zechmeister, M., & Kürster, M. 2009, *A&A*, **496**, 577
- Zechmeister, M., Anglada-Escudé, G., & Reiners, A. 2014, *A&A*, **561**, A59
- Zink, J. K., Hardegree-Ullman, K. K., Christiansen, J. L., et al. 2021, *AJ*, **162**, 259

¹ Centro de Astrobiología (CAB), CSIC-INTA, ESAC campus, Camino Bajo del Castillo s/n, 28692 Villanueva de la Cañada, Madrid, Spain

² Center for Astrophysics | Harvard & Smithsonian, 60 Garden Street, Cambridge, MA 02138, USA

³ Department of Physics, University of Warwick, Gibbet Hill Road, Coventry, UK

⁴ Center for Exoplanets and Habitability, University of Warwick, Gibbet Hill Road, Coventry, UK

⁵ Dipartimento di Fisica, Università degli Studi di Torino, Via Pietro Giuria, 1, 10125 Torino, Italy

⁶ Dept. of Physics & Astronomy, Swarthmore College, Swarthmore, PA 19081, USA

⁷ Instituto de Astrofísica e Ciências do Espaço, Universidade do Porto, CAUP, Rua das Estrelas, 4150-762 Porto, Portugal

⁸ Centro Astronómico Hispano en Andalucía, Sierra de los Filabres sn, 04550 Gérgal Almería, Spain

⁹ Komaba Institute for Science, The University of Tokyo, 3-8-1 Komaba, Meguro, Tokyo 153-8902, Japan

¹⁰ Astrobiology Center, 2-21-1 Osawa, Mitaka, Tokyo 181-8588, Japan

¹¹ Instituto de Astrofísica de Canarias (IAC), 38205 La Laguna, Tenerife, Spain

¹² Institut für Planetenforschung, Deutsches Zentrum für Luft- und Raumfahrt, Rutherfordstr. 2, 12489 Berlin, Germany

¹³ National Astronomical Observatory of Japan, 2-21-1 Osawa, Mitaka, Tokyo 181-8588, Japan

¹⁴ Department of Space, Earth and Environment, Chalmers University of Technology, Onsala Space Observatory, 43992, Sweden

¹⁵ Leiden Observatory, University of Leiden, PO Box 9513, 2300 RA Leiden, The Netherlands

¹⁶ Thüringer Landessternwarte Sternwarte 5, D-07778 Tautenburg, Germany

¹⁷ Sub-department of Astrophysics, Department of Physics, University of Oxford, Oxford OX1 3RH, UK

¹⁸ Department of Astronomy and Astrophysics, University of California, Santa Cruz, CA 95060, USA

Appendix A: Ancillary analysis

A.1. Spectroscopic analysis

The equivalent widths (EW) were consistently measured on the combined HARPS spectrum using the ARES code¹⁵ (Sousa et al. 2007, 2015) for the list of lines presented in Sousa et al. (2008). The best set of spectroscopic parameters for each spectrum was found by using a minimization process to find the ionization and excitation equilibrium. This process makes use of a grid of Kurucz model atmospheres (Kurucz 1993) and the latest version of the radiative transfer code MOOG (Snedden 1973). We also derived a more accurate trigonometric surface gravity using recent *Gaia* data following the same procedure as described in Sousa et al. (2021) which provided a consistent value when compared with the spectroscopic surface gravity.

The derived parameters from this study are shown in Table C.3. As a double-check, we also estimated the fundamental stellar parameters by using the TRES spectra and the Stellar Parameter Classification (SPC). We also used the param v1.3¹⁶ code for stellar parameter estimation (da Silva et al. 2006). The results of this code after inputting the effective temperature and metallicity from the ARES+MOOG spectroscopic analysis, provide an age of 3.836 ± 0.645 Gyr, a mass and radius of $1.291 \pm 0.048 M_{\odot}$ and $1.689 \pm 0.093 R_{\odot}$ and a surface gravity of 4.066 ± 0.044 dex. These values are compatible within the uncertainties with those from the empirical relations from Torres et al. (2010).

In all cases, the results are compatible with those from the co-added HARPS spectrum, which is used throughout the paper as our reference set of parameters.

A.2. Spectral energy distribution

We analyzed the broad-band photometry with the aim to constrain and test the hierarchical eclipsing binary (HEB) scenarios proposed for the configuration of the EPIC 248472140 system. In practice, two scenarios have been proposed in this work for the eclipsing binary: a pair of similar mass mid-to-late M-dwarfs (labelled hereafter as G1+M5+M5) or a K7/M0 star plus a brown dwarf (labelled as G1+K7+BD). Given the slight differences in the spectral types, we investigated if this could be reflected in the SED.

To this end, we built spectra based on the NextGen spectral models (Hauschildt et al. 1999). In order to weight the contribution of each stellar model to the composite SED for a given combination of objects, the stellar fluxes (which are given in the models in units of $\text{erg cm}^{-2} \text{s}^{-1} \text{\AA}^{-1}$) were multiplied by the corresponding radii squared. The parameters (T_{eff} , $\log g$, R_{\star}) of the models were: G1 V (5863 K, 4.06 dex, $1.57 R_{\odot}$), K7 V (4100 K, 4.65 dex, $0.63 R_{\odot}$), M5 V (3060 K, 5.07 dex, $0.196 R_{\odot}$). The parameters for the G1V component come from a spectroscopic determination from the HARPS spectrum (see Sect. 2.6); while the parameters for the K7V and M5V were taken from the table of stellar parameters by Mamajek¹⁷; and for the brown dwarf the parameters were chosen to be 1000 K, $\log g = 5.50$, $R = 0.10 R_{\odot}$. A slight reddening $E(B-V) = 0.036$ was applied to all models. The value was estimated by comparing the observed $B-V = 0.658$ with the intrinsic colour of a G1 V star, 0.622.

¹⁵ The last version, ARES v2, can be downloaded at <https://github.com/sousasag/ARES>

¹⁶ <http://stev.oapd.inaf.it/cgi-bin/param>

¹⁷ https://www.pas.rochester.edu/~emamajek/EEM_dwarf_UBVIJHK_colors_Teff.txt

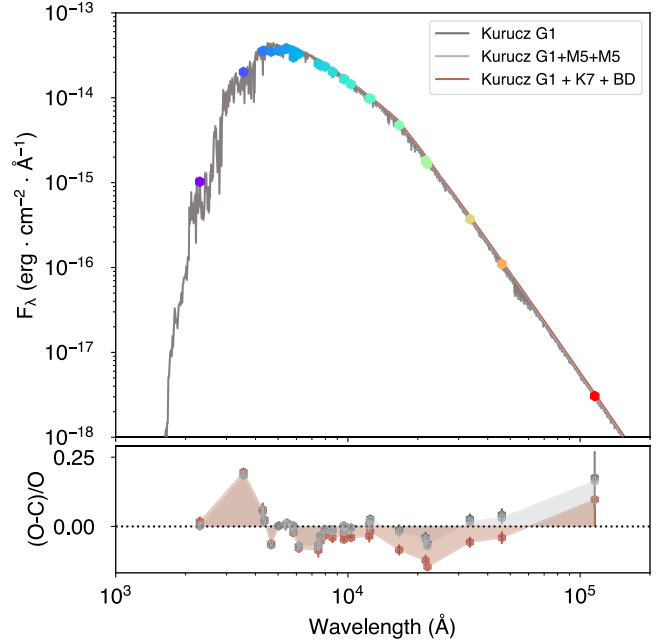


Fig. A.1. Spectral energy distribution of EPIC 248472140. The observed fluxes are shown as colored symbols (coded by their wavelength) and the composite model of a G1 dwarf and two M5 dwarfs from the Kurucz sample of spectral models is shown in gray. The model has been normalized to the observed flux in the Ks band.

Figure A.1 (top panel) shows the broad band photometry together with the two proposed models (G1+K7+BD and G1+M5+M5) also compared to a simple model of a single G1-dwarf. We scaled each model using the optical bands (filters with effective wavelength shorter than 7000 \AA) and determined the scaling factor through a least-squares methodology. To better visualize the differences between the models, we computed the synthetic photometry of the models at the observed bands by using the "Carlos Rodrigo" Filter Profile Service offered by the Spanish Virtual Observatory (Rodrigo et al. 2012; Rodrigo & Solano 2020; Rodrigo et al. 2024). The lower panel in Fig. A.1 shows the relative difference between the synthetic photometry from each model and the observed broad-band photometric measurements. As shown in this figure, the G1+K7+BD produces an infrared excess significantly larger than that observed in the data (red shaded region). By contrast, the G1+M5+M5 model is indistinguishable from the single G1 dwarf model and very much compatible with the observed data. Consequently, although the SED does not provide sufficient evidence to directly confirm the G1+M5+M5 scenario when compared to the G1 model based on the Occam's razor, it allows us to discard the G1+K7+BD configuration.

A.3. Analysis of the multi-band transit photometry

The strongly color-dependent transit (eclipse) depths from our MuSCAT3 data shown in Fig. 1 point to a significant amount of blending light from a star unrelated to the eclipsing pair. To model this, we fit an eclipse model to all four bands simultaneously. Our model uses the same orbital and stellar parameters for the light curves in all four bands. The only differences are band-appropriate limb darkening, independent detrending for the four light curves, and a per-band free parameter that represents the amount of blending light in that filter, relative to the intrinsic flux

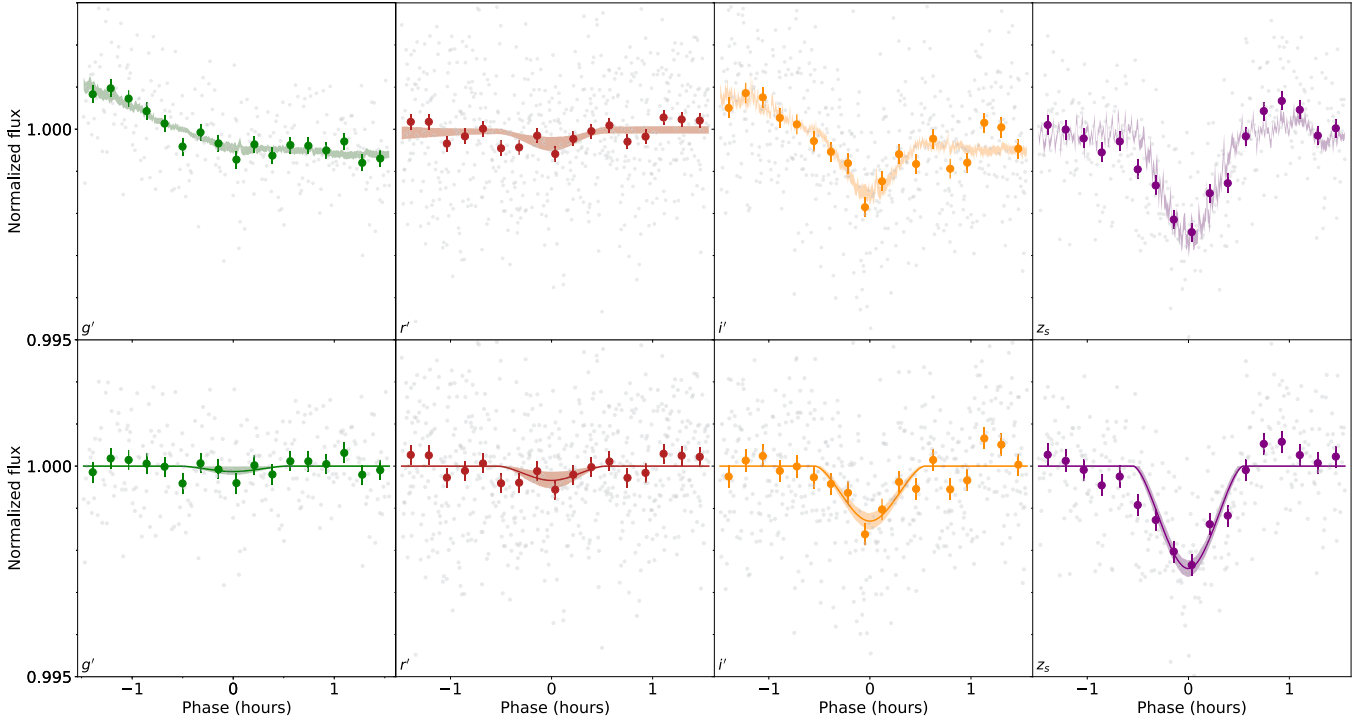


Fig. A.2. Modeling of the MuSCAT3 light curves for all four bands, from left to right: g , r , i , z_s . Top panels show the raw light curves, while bottom panels show the detrended light curves and the corresponding model (all done in a simultaneous fit). The shaded areas around the fit lines are the 68.3% credible interval in the MCMC.

from the eclipsing pair. By looking at how the required amount of diluting light varies with wavelength, we can infer some of the properties of the eclipsing system, especially since we know the stellar characteristics of the dominant star (see Sect. A.1).

Based on the results from the RV analysis in Sect. 3.1, we set a Gaussian prior on the stellar radius ratio with a mean of 1.0 and a standard deviation of 0.1. Imposing the assumption of nearly-equal-mass (and thus presumably equal effective temperature) stars allows us to also assume that the eclipse depth is intrinsically wavelength-independent, and to attribute the observed depth differences to the blending light. We build the model and sample the posterior of the parameters using the Python package *exoplanet* (Foreman-Mackey et al. 2021a,b), which uses Hamiltonian Monte Carlo with the No U-Turn Sampler (Hoffman & Gelman 2014), as implemented in PyMC3 (Salvatier et al. 2016). We ran seven independent chains with 1500 tuning steps and 3000 sampling steps each. For every parameter of interest, the \hat{R} statistic (Gelman & Rubin 1992) was less than 1.001, indicating convergence of the sampler. The resulting models and detrended light curves are shown in Fig. A.2.

Based on this analysis we can focus on the posterior distributions of the band-dependent dilution parameters. These results are shown in the violin plots in Fig. A.3. Since the amount of blending light is specified relative to the continuum of the light curve, it essentially gives the flux ratio between the eclipsing system and the blend in that band. Hence, we overplot what we would expect if the blending light is from a G1V star, and the eclipsing system is an M5+M5.5. We use colors and absolute magnitudes from Covey et al. (2007), with a small correction from SDSS z' to Pan-STARRS z_s (Tonry et al. 2012). As shown in the figure, this scenario agrees well with the observations. We

note that an M5+M5 model is also compatible, but with the z_s band presenting a slightly larger difference ($\gtrsim 1\sigma$).

In order to test the G1+K7+BD/planet scenario described in Appendix A.5, we perform a similar analysis but in this case we restrict the radius ratio between the eclipsing components (i.e., R_C/R_B) to a maximum of 0.2. Although the results show that the data could still come from such model, the solution is quite marginal, with the model preferring both the $r'-i'$ and $i'-z'$ colors of the companion to be redder than a K7 or M0 star. Hence, based on the analysis of the multi-color eclipse MuSCAT3 data, the scenario composed of a G1 plus two similar-mass mid-type M-dwarfs seems to be preferred.

A.4. Spectroscopic indicators

The HARPS data were also reduced with the HARPS-TERRA pipeline (Anglada-Escudé & Butler 2012), which provides additional indicators based on specific spectral lines related to stellar activity like the S-index, $H\alpha$ or the sodium doublet lines. In this case, the average uncertainty of this dataset is 4.4 m/s with a dispersion in the uncertainties of 1.8 m/s. Given the larger consistency among the uncertainties from the DRS extraction, we use that RV time series in this paper (see Sect. 2.2).

From the time series of the indicators from both the DRS and the HARPS-TERRA pipelines, we built the Generalized Lomb-Scargle (GLS) periodograms (Zechmeister & Kürster 2009) to look for correlations of these indicators with the periodicity of the eclipsing object. This is shown in Fig. A.4, where we find no significant variations neither in the CCF asymmetry (BIS and FWHM) nor in the activity signal. Consequently, we can conclude that the star causing the effects is not eclipsing the main star EPIC 248472140 A.

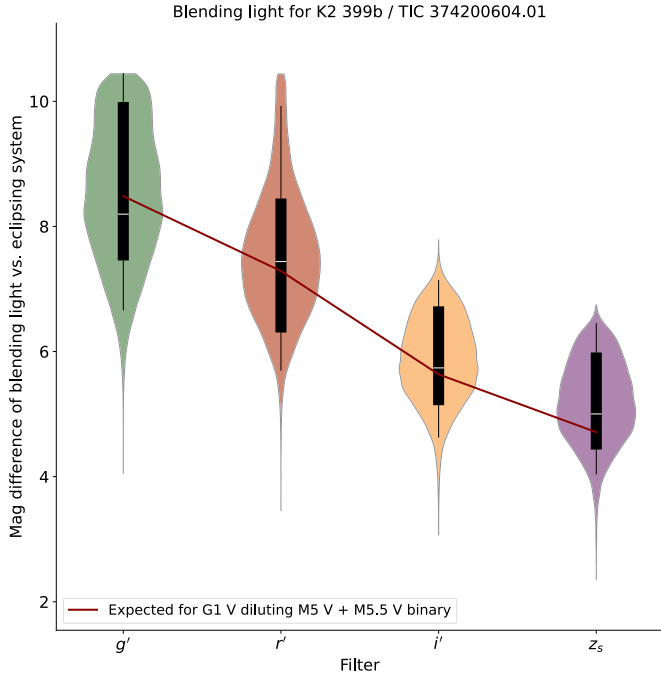


Fig. A.3. Posterior distribution of the dilution factors (flux ratios between blending light and flux of the eclipsing system) for the four bands of the MuSCAT3 observations, expressed in magnitudes. The central black box shows the 68.3% credible interval with the median marked as a white line, and the larger solid lines represent the 95.4% credible interval. The surrounding color shows the posterior distributions from the MCMC run. The solid line shows the expected flux of a G1 V star in each band compared to a pair of M5 V stars (see text for details).

However, given the complexity of the system, we explore the phase-folded diagram of the FWHM with the period of the binary. This is shown in Fig. A.5, where we have added a toy sinusoidal model as a dotted line to guide the eye. Even though the significance is still low, there seems to be a sinusoidal pattern in this diagram with an amplitude around 10 m/s. This small amplitude might be explained by an additional CCF corresponding to the combination of both B and C components. Interestingly, this dependency is enhanced when we only focus on the dataset from the 2023 campaign, when the binary was close to a quadrature of the orbit and hence the separation from the CCF of the main target is maximized. However in the 2018 dataset, the CCF of star A and the CCF of $B+C$ are closer to conjunction and hence the signature in the FWHM is minimized. Indeed, if we focus on the filled symbols (the 2023 campaign), we see a larger phase dependency of the FWHM than in the opened symbols. This suggests that a second CCF coming from the combined $B+C$ binary is also somehow present in the spectra.

Additionally, and more interestingly, one spectrum from HARPS (2023 campaign) was obtained during the eclipse of the binary (the symbol close to phase $\phi = 1$ in Fig. A.5). This symbol is significantly below the expected value. This decrease in the FWHM of the global CCF of the system can easily be explained if we think of it as suppressing or at least fading the CCF corresponding to the $B+C$ binary as one of the components is being eclipsed and stops contributing to the global CCF itself, hence making the global CCF slightly sharper.

As a double check, we have also used the CARMENES data from the night that we observed the system during one of

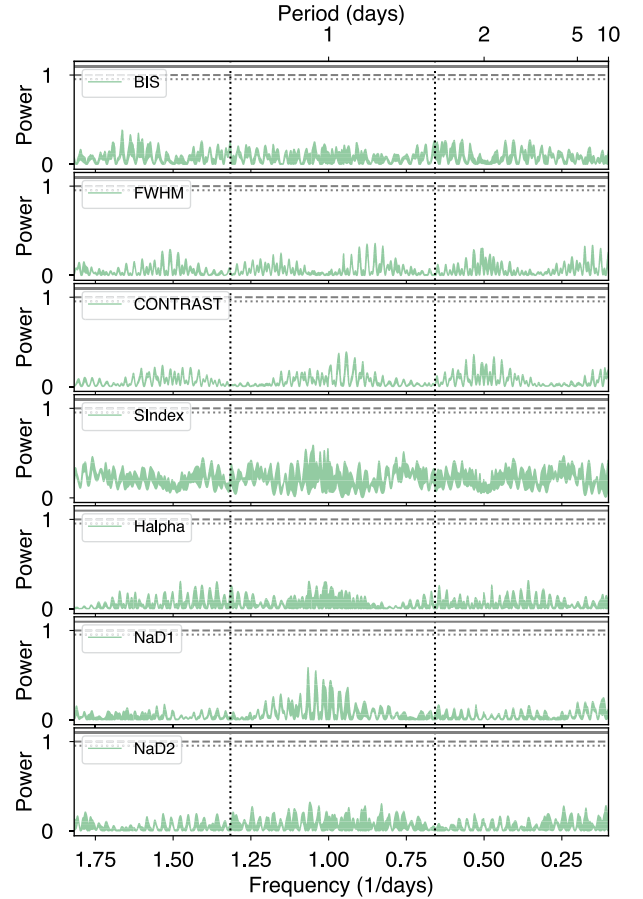


Fig. A.4. Generalized Lomb-Scargle (GLS) periodogram of the activity indicators from the HARPS observations as determined from the HARPS-TERRA pipeline. The vertical dotted lines indicate the 0.76 days and twice this period (1.52 days). False alarm probabilities of 1%, 5%, and 10% are indicated with horizontal dotted, dashed and solid lines, respectively.

the eclipses. In this case, the observations were also performed close to a quadrature, and so we should see a decrease in the FWHM during the eclipse. Since the effect is very subtle, we perform another extraction of the CCF but now cross-correlating the spectra with an M2 mask instead of an F9. Figure A.6 shows this analysis. Again, while in this case we cannot appreciate a smaller in-eclipse FWHM for the data from the CCF corresponding to the F9 mask (open symbols), it is very clear in the case of the M2 mask (filled symbols). Indeed, the decrease in the CCF FWHM is more abrupt in this case with the M2 mask than in the HARPS case. This is in fact what one would expect if the binaries are indeed of late spectral types, since the weight of the $B+C$ CCF against the CCF from the A component is larger.

However, despite all these indications, it is important to highlight that the significance of these signals is still too low to be considered as a clear evidence of the similar-mass scenario for B and C . However, it adds support to the already discussed and favored scenario using other techniques.

A.5. Eclipsing binary configuration

In Sect. 4, we proposed two scenarios to explain the absence of a secondary eclipse in the phase-folded diagram with a ~ 0.76 day periodicity in the preferred G1+M5+M5 scenario.

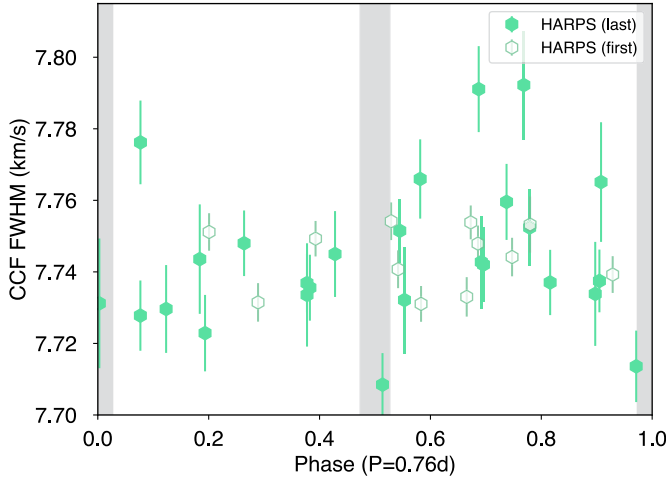


Fig. A.5. Full-width at half-maximum (FWHM) of the cross-correlation function from the HARPS dataset phase folded with a 0.76-day period. Open symbols represent HARPS data obtained in the first campaign (in 2018), while filled symbols represent data from the last campaign (in 2023). The gray shaded regions show the location of the primary and secondary eclipses assuming a circular orbit for the binary.

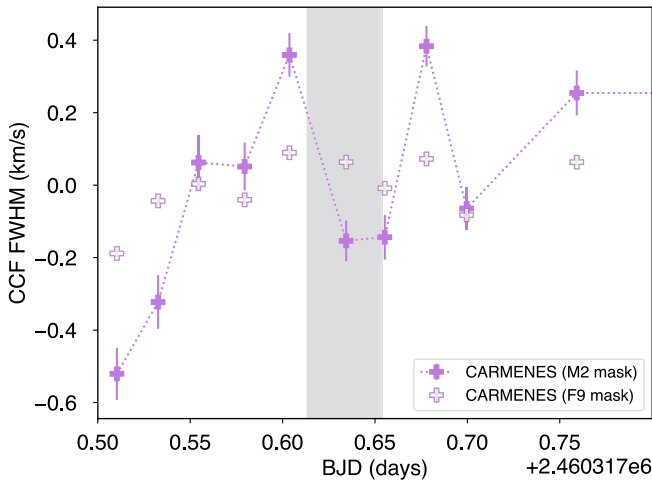


Fig. A.6. Full-width at half-maximum (FWHM) of the cross-correlation function from the CARMENES time series for the night of 7-February-2024. Open symbols represent CARMENES CCFs obtained with the F9 mask (close to the spectral type of component A), while filled symbols represent CARMENES CCFs extracted by using an M2 mask (closer to the B + C components). The dotted lines simply connect the datapoints from the M2 mask dataset to guide the eye. The gray shaded region shows expected time of the primary eclipse.

The first option (eccentric orbit of the B+C pair) allows any mass repartition among the B and C components. However, a 0.76-day period binary seems unlikely to have an orbit sufficiently eccentric as to prevent the secondary eclipse from occurring. Still, the large impact parameter keeps this possibility for eccentricities larger than around 0.15. However, for such a short period, these values seem unlikely.

The second option (a twin pair of mid-M-dwarfs at twice the published period) is the most plausible from the data in hand. This alternative implies that the actual period is ~ 1.52 days. Indeed, in Fig. B.4, we plot the TESS photometry from the SPOC pipeline (using the PDC_SAP flux) phase-folded with twice the reported period. As shown, there is also some evi-

dence of differences in the depth of the odd-even eclipses (i.e., at phases $\phi = 0.0$ and $\phi = 0.5$ in the figure), however it is still not significant enough (180 ± 135 ppm) to be used as a claim.

We thus conclude that the most plausible scenario for this system is a hierarchical eclipsing binary where the brightest component (A) is a G1 dwarf, which is orbited in a 847 days period by a pair of mid-type M-dwarfs producing eclipses every 1.52 days. We note that under this scenario, the periodicity of the FWHM shown in Fig. A.5 still holds because of the similar properties of both eclipsing components, making the width of the CCF to vary on a half-orbital-period rhythm.

A.6. Alternative validation techniques

An independent validation pipeline, known as RAVEN, is currently under development (Hadjigeorgiou et al in prep). RAVEN is an adaptation of the machine-learning based *Kepler* validation tool presented in Armstrong et al. (2021) to the *TESS* mission, and incorporates as part of the pipeline positional probabilities for true candidate host stars published in Hadjigeorgiou & Armstrong (2023). We applied RAVEN to TOI-4838/K2-399 using *TESS* lightcurve data supported by *Gaia* information, including nearby sources and RUWE values. The results are in strong agreement with the HEB scenario favoured by direct observations, finding a probability $> 99.9\%$ that the candidate is a HEB in a direct Planet vs HEB test. Given that RAVEN is still under development we do not take this as evidence by itself, but note it in support of the scenario proposed from the above observations. It is also highly interesting that different validation pipelines on different datasets (here *TESS* vs *K2*) can give starkly different results, as noted by Armstrong et al. (2021). This discrepancy is perhaps not surprising, particularly considering different datasets, but should be more clearly recognised when considering the status of validated planets in the context of the wider exoplanet population.

A.7. Concerns on the validation process

Although we acknowledge the fact that this is a special case, it clearly evidences the need to properly establish the criteria for planet confirmation and signal verification. In this context, a community proposal is being discussed (the Exoplanet Confirmation Protocol, ECP) to decide upon the necessary criteria to consider a signal as a true confirmed planet. One of the key steps in this discussion is the verification of the origin of the signal, especially in the case of signals detected through the transit method that cannot be further followed-up with radial velocities due to a shallow RV signature or faint host star. In those cases, the community has opted for the so-called validation technique, based on discarding all other possibilities causing the light curve dimming that are not of planetary origin.

In the case of K2-399 b, the authors in Christiansen et al. (2022) used the *vespa* python module¹⁸. This module computes the individual probabilities of four different non-planetary scenarios that could mimic the observed transit signal. These are the eclipsing binary (EB), the background eclipsing binary (BEB), the hierarchical eclipsing binary (HEB), and the case of a blended star hosting an actual planet with different properties (B1p). For the particular case of K2-399 b, we have found that the actual scenario corresponds to a HEB. The probability of this

¹⁸ As of 2023 (i.e., after the publication of the validation paper), the *vespa* algorithm was retired (and no longer maintained) in favor of *triceratops* (Giacalone et al. 2022), see Morton et al. (2023).

scenario as reported in Christiansen et al. (2022) is 1.54×10^{-4} . Such a low probability of this scenario is unlikely to be accurately calculated given the evidence provided in this work. This points to either an underestimate of the capability of the K2 light curve to constrain the transit shape, an underestimated a priori probability for the HEB scenario in the validation software in the absence of additional follow-up data (e.g. multi-color photometry or RVs), or an error in consideration of the evidence from ancillary data during the validation process (e.g. the large RUWE or the slight difference in the odd/even eclipse depths).

Overall, we highlight that published planets from validation processes, whether in bulk or individually, may still contain false positives. Indeed, if a 99% probability threshold is used, naively we should expect 1 in 100 validated planets to be false. On this basis, we encourage the developers of such codes to pay particular attention to the a priori probabilities and all available evidence. Additionally, testing validation results against as wide an array of alternatives as possible, whether different validation tools or independent follow-up, should be prioritised. Further, we encourage owners of exoplanet catalogues to distinguish validated planets from ‘confirmed’ planets where possible.

Appendix B: Figures

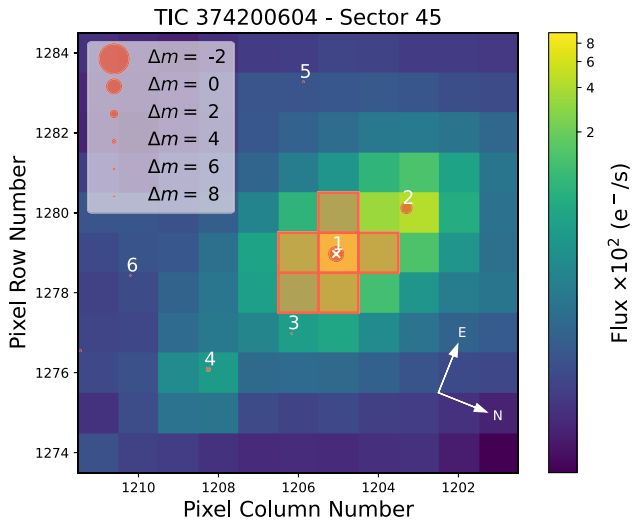


Fig. B.1. Target Pixel File (TPF) of EPIC 248472140 (also known as TIC 374200604) from the TESS mission. The figure, created with the `tpfplotter` tool (Aller et al. 2020), shows the location of the target (white cross symbol) as well as the photometric aperture used by SPOC pipeline to extract the photometry (red shaded region) and the nearby *Gaia* sources (red circles with size scaled with the contrast magnitude against the main target).

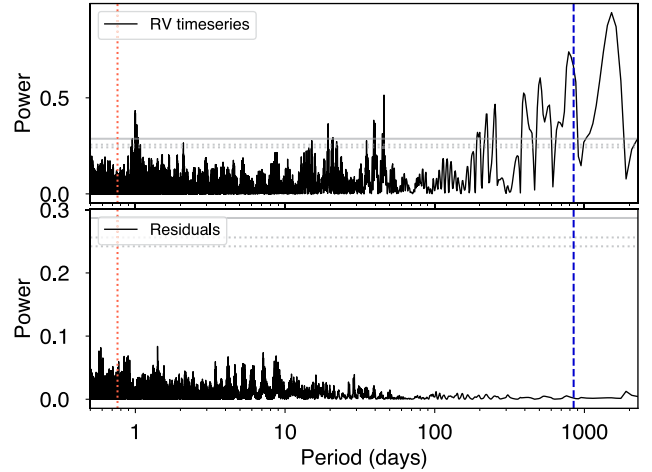


Fig. B.2. **Top panel:** Generalised Lomb-Scargle (GLS) periodogram of the RV time series from the TRES, HARPS and CARMENES instruments (assuming no instrumental offset). The vertical red dotted line indicates the reported transit period, while the vertical blue dashed line shows the converged periodicity of the RV data (see Sect. 3). **Bottom panel:** GLS of the residuals after subtracting the median RV model obtained in Sect. 3. In both panels, the horizontal dotted lines are the 1% and 5% false alarm probability (FAP) levels while the solid line corresponds to the 0.1% FAP level.

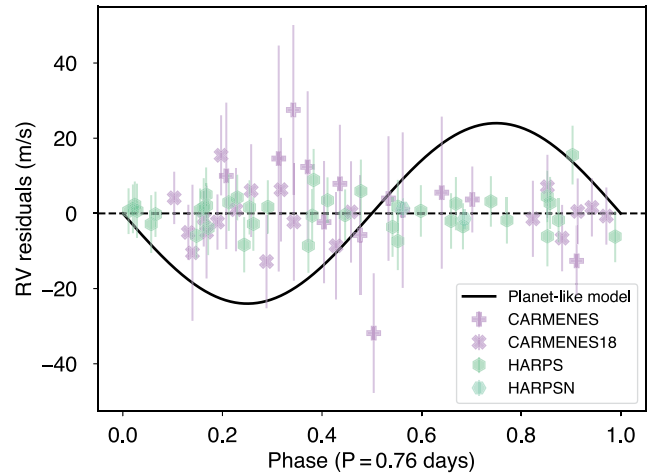


Fig. B.3. Phase-folded CARMENES and HARPS radial velocities after subtracting the long-period keplerian model. The expected signal of the validated planet as estimated by Christiansen et al. (2022) is shown as a solid black line.

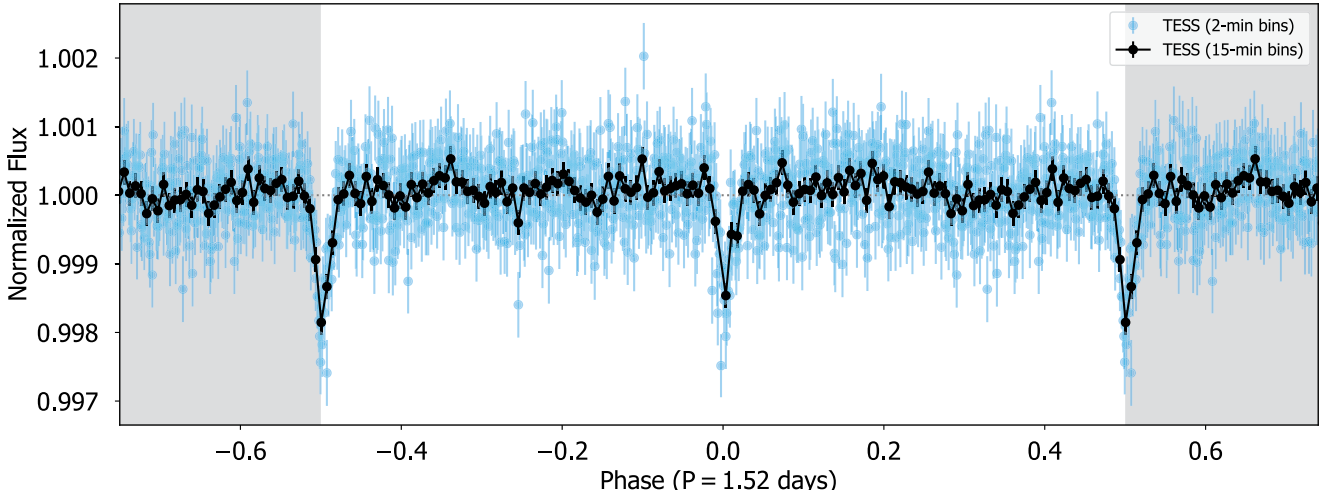


Fig. B.4. TESS photometry folded with a period of 1.52 days (from the analysis of the multi-color band in Sect. 3.2), corresponding to twice the reported period from the K2 discovery in Zink et al. (2021). Two different binnings are shown corresponding to equivalent sizes of 2 minutes (blue symbols) and 15 minutes (black symbols). A slightly different depth is apparent between phases $\phi = 0.0$ and $\phi = 0.5$, thus enhancing the similar-type low-mass star scenario for the eclipsing binary (see Sect. 4).

Appendix C: Tables

Table C.1. Radial velocity measurements of EPIC 248472140. Only the first five rows are shown. This table is available in its full format at CDS.

BJD (TDB)	RV (km/s)	σ_{RV} (km/s)	Instrument
2458172.66425265	25.5833	0.0059	HARPS
2458172.74227421	25.5840	0.0059	HARPS
2458172.78903391	25.5852	0.0060	HARPS
2458174.6535619	25.5385	0.0061	HARPS
2458174.72069192	25.5386	0.0061	HARPS
...			

Table C.2. Broad-band photometry from EPIC 248472140

Band	Wavelength (Å)	Flux $\times 10^{-14}$ (erg · cm $^{-2}$ · s $^{-1}$ · Å $^{-1}$)
GALEX.NUV	2303.4	0.1026 ± 0.0018
Johnson.U	3551.1	2.013 ± 0.031
APASS.B	4299.2	3.562 ± 0.092
Johnson.B	4369.5	3.559 ± 0.012
SDSS.g	4671.8	3.491 ± 0.013
GAIA3.Gbp	5035.8	3.5710 ± 0.0095
APASS.V	5393.9	3.805 ± 0.081
Johnson.V	5467.6	3.799 ± 0.011
ACS_WFC.F606W	5809.3	3.5532 ± 0.0051
GAIA3.G	5822.4	2.9889 ± 0.0076
SDSS.r	6141.1	3.295 ± 0.059
Johnson.R	6695.8	3.2724 ± 0.0068
SDSS.i	7457.9	2.523 ± 0.066
GAIA3.Grp	7620.0	2.4036 ± 0.0084
ACS_WFC.F814W	7973.4	2.3314 ± 0.0036
Johnson.I	8568.9	2.3715 ± 0.0039
GAIA3.Grvs	8578.2	2.026 ± 0.039
PS1.y	9613.6	1.6760 ± 0.0051
PS1.y	9613.6	1.6481 ± 0.0098
UKIDSS.Y	10305.0	1.44498 ± 0.00091
2MASS.J	12350.0	0.982 ± 0.022
UKIDSS.J	12483.0	0.97965 ± 0.00051
UKIDSS.H	16313.0	0.42307 ± 0.00027
2MASS.H	16620.0	0.4745 ± 0.0096
2MASS.Ks	21590.0	0.1819 ± 0.0039
UKIDSS.K	22010.0	0.16633 ± 0.00014
WISE.W1	33526.0	0.03719 ± 0.00076
WISE.W2	46028.0	0.01099 ± 0.00025
WISE.W3	115608.0	0.000306 ± 0.000029

Table C.3. Spectroscopically derived stellar parameters of EPIC 248472140 A from both the HARPS co-added spectrum using the ARES+MOOG methodology and the TRES spectra using the SPC algorithm (see Sect. 2.6)

Parameter	ARES+MOOG	SPC
T_{eff} (K)	5863 ± 62	5726 ± 130
$\log g$ (dex,cgs)	4.05 ± 0.11	4.12 ± 0.15
[Fe/H]	0.335 ± 0.014	0.43 ± 0.08
v_{turb} (km/s)	1.111 ± 0.022	-
$v \sin i$ (km/s)	-	5.5 ± 1.2
$M_{\star,A}$ (M_{\odot})	1.31 ± 0.03	-
$R_{\star,A}$ (R_{\odot})	1.57 ± 0.05	-

Table C.4. Prior and posteriors for the RV analysis of EPIC 248472140 presented in Sect. 3.

Parameter	Prior [†]	Posterior
Orbital period, P_B [days]	$\mathcal{U}(2,1000)$	$846.62^{+0.22}_{-0.28}$
Time of conjunction, $T_{0,B} - 2400000$ [days]	$\mathcal{U}(59551,60551)$	$59684.31^{+0.72}_{-0.85}$
RV semi-amplitude, K_B [m/s]	$\mathcal{U}(0,100000)$	8901^{+38}_{-50}
Orbital eccentricity, e_B	$\mathcal{U}(0,0.9)$	$0.4919^{+0.0021}_{-0.0020}$
Arg. periastron, ω_B [deg.]	$\mathcal{U}(-180,180)$	$-49.59^{+0.23}_{-0.19}$
δ_{CARMENES} [km/s]	$\mathcal{T}(27.7,0.3,27,28.5)$	$27.756^{+0.066}_{-0.057}$
δ_{HARPS} [km/s]	$\mathcal{T}(27.7,0.3,27,28.5)$	$27.905^{+0.032}_{-0.042}$
δ_{HARPSN} [km/s]	$\mathcal{T}(27.7,0.3,27,28.5)$	$27.902^{+0.032}_{-0.041}$
δ_{TRES} [km/s]	$\mathcal{T}(27.7,0.3,27,28.5)$	$27.919^{+0.033}_{-0.033}$
σ_{CARMENES} [m/s]	$\mathcal{U}(-2.5,3.5)$	$1.0^{+6.4}_{-5.6}$
σ_{HARPS} [m/s]	$\mathcal{U}(-2.5,3.5)$	$0.5^{+4.2}_{-3.2}$
σ_{HARPSN} [m/s]	$\mathcal{U}(-2.5,3.5)$	$0.9^{+8.3}_{-5.2}$
σ_{TRES} [m/s]	$\mathcal{U}(-2.5,4.0)$	$8.8^{+4.9}_{-2.2}$
<i>Derived parameters</i>		
Minimum mass, $m_B \sin i_B$ [M_{J}]	(derived)	0.4130 ± 0.0066
Orbit semi-major axis, a_B [AU]	(derived)	$1.916^{+0.014}_{-0.015}$
Relative orbital separation, a_B/R_{\star}	(derived)	$262.5^{+8.8}_{-8.3}$
Stellar effective incident flux, S_B [S_{\oplus}]	(derived)	$0.710^{+0.057}_{-0.054}$
Stellar luminosity, L_{\star} [L_{\odot}]	(derived)	$2.61^{+0.20}_{-0.19}$

Notes. [†]Prior distributions are defined as: $\mathcal{U}(a, b)$ for a uniform distribution between a and b , and $\mathcal{T}(\mu, \sigma, a, b)$ for a normal distribution with mean μ and standard deviation σ constrained between values a and b (the so-called truncated Gaussian).

Table C.5. Prior and posteriors for the multi-band photometry analysis of EPIC 248472140 presented in Sect. A.3.

Parameter	Prior [†]	Posterior
Eclipsing system orbital period, P_c [days]	$\mathcal{N}(1.520017, 0.0000002)$	$1.5200154^{+0.0000010}_{-0.0000016}$
Time of mid-transit, $T_{0,c} - 2400000$ [days]	$\mathcal{N}(59578.996, 0.002)$	59578.995 ± 0.001
Impact parameter, b	$\mathcal{U}(0,1.5)$	$1.46^{+0.04}_{-0.48}$
Radius ratio, R_C/R_B	$\mathcal{T}(1.0, 0.1, 0.5, 2.0)$	$1.00^{+0.09}_{-0.12}$

Notes. [†]Notation for prior distributions is the same as used in Table C.4, with the addition of $\mathcal{N}(\mu, \sigma)$ to denote a normal distribution with mean μ and standard deviation σ .